Upscale and downscale energy transfer over the tropical Pacific revealed by scatterometer winds

Gregory P. King[1,2], Jur Vogelzang[3] and Ad Stoffelen[3]

[1]Centro de Geofisica - IDL, Campo Grande, Edificio C8, Universidade de Lisboa, P-1749-016 Lisboa, Portugal.

[2]Instituto Gulbenkian de Ciencia, Apartado 14, 2781-901 Oeiras, Portugal.

[3]KNMI Royal Netherlands Meteorological Institute, PO Box 201, 3730 AE De Bilt, The Netherlands.

Corresponding author: Jur Vogelzang, KNMI Royal Netherlands Meteorological Institute, PO Box 201, 3730 AE De Bilt, The Netherlands. (jur.vogelzang@knmi.nl)

Abstract

According to two-dimensional turbulence theory, the sign of the third-order structure function D_3 identifies the direction of energy transfer, with $D_3 < 0$ implying downscale transfer and $D_3 > 0$ upscale transfer. Using near-surface winds inferred from radar backscatter measurements by SeaWinds-on-QuikSCAT and ASCAT-on-MetOp-A scatterometers, third-order structure functions D_{3a} (where the subscript a indicates the along-track direction) were calculated for both rainy and dry regions in the tropical Pacific. The skewness S_a was found to asymptote to an approximate constant value when the separation variable r exceeded 200 - 300 km. The time evolution of S_a was followed using its value at 300 km, and was found to vary in regionally and seasonally in magnitude and sign. Fluxes were calculated using the third-order structure function law and split into upscale (where velocity differences $\delta u_{La} > 0$) and downscale (where $\delta u_{La} < 0$) components. The variability in magnitude and sign was shown to be due to the changing relative strength of convergence and divergence within a region. Thus our main result may be expressed as follows. Energy fluxes (i) downscale where and when surface convergence (deep convection) dominates, (ii) upscale where and when surface divergence dominates, and (iii) have both large upscale and downscale components in regions frequented by mesoscale convective systems. The link with surface convergence and divergence challenges the usual picture of mesoscale turbulence as either a 2D or 3D energy cascade.

1 Introduction

This paper addresses a long-standing question in atmospheric dynamics: Is horizontal kinetic energy transferred to small scales through a downscale cascade as in ideal three-dimensional (3D) turbulence? Or is it transferred to large scales via a two-dimensional (2D) inverse cascade? The classic papers by *Nastrom et al.*[1984] and *Nastrom and Gage* [1985] and more recent papers by *Lindborg* [1999] and *Cho and Lindborg* [2001] have addressed this question through an analysis of global datasets of winds near the tropopause measured by instruments carried on commercial aircraft. Here we use winds at the bottom of the marine boundary layer inferred from radar backscatter from the ocean surface measured by the Advanced Scatterometer (ASCAT) on the MetOp-A satellite and the SeaWinds scatterometer on the QuikSCAT satellite.

Nastrom et al. [1984] calculated horizontal wind spectra and demonstrated that they follow a k^{-3} power law at large scales ($r > 1000$ km) and transition to a $k^{-5/3}$ power law at small scales ($2 < r < 200$ km). The k^{-3} range is consistent with Charney's theory of quasigeostrophic turbulence [*Charney,* 1971]. The origin of the $k^{-5/3}$ range, however, continues to be debated. Two types of theories have been put forth. One is based on internal gravity wave dynamics [*Dewan*, 1979;*VanZandt*, 1982; *Dewan*, 1997], which predicts a downscale cascade of energy from longer to shorter waves. The other is based on 2D and geostrophic turbulence [*Gage*, 1979; *Lilly*, 1983]. The basic picture of the latter theory is that geophysical constraints (stratification, rotation, thin atmosphere) decouple atmospheric motions into layers and energy sources at large-scale (e.g., baroclinic instability) and small-scale (e.g., convection and shearing instabilities). These give rise to a combined energy and enstrophy inertial range that yields a $k^{-5/3}$ range at small-scales and a k^{-3} range at large-scales [*Lilly*, 1989]. This 2D-like or stratified turbulence scenario implies an upscale energy cascade, whereas the gravity wave theory predicts a downscale cascade.

Scatterometer wind spectra are similar to the upper level spectra over the large mesoscale and transition regions. *Freilich and Chelton* [1986], *Wikle et al.* [1999], *Patoux and Brown* [2001], and *Xu et al.* [2011] found power laws (for scales down to 200 km) varying between $k^{-1.9}$ and $k^{-2.9}$, with the shallowest spectra in the tropical Pacific and Atlantic, becoming steeper towards the poles, but with the steepest in the tropical Indian Ocean. Due to noise and processing issues, accurate power laws for scales below 200 km remain a challenge [*Rodriguez and Chau*, 2011; *King* et al.,2013]. *Wikle* [1999] expanded their analysis to smaller scales using high-resolution retrievals of 10-m winds from Doppler radar measurements carried on research aircraft. Their results were obtained using observations covering a domain in the tropical western Pacific in austral summer during the Tropical Ocean Global Atmosphere Coupled Ocean-Atmosphere Response Experiment (TOGA COARE) intensive observation period (IOP). For the combined spectra, they found a $k^{-5/3}$ power law down to 1 km. The $k^{-5/3}$ power law was noted to be consistent with an upscale energy cascade driven by an energy source at high wave numbers thought to be associated with organized tropical convection.

The inability of the energy spectrum to distinguish between different theories led *Lindborg* [1999] to develop a test based on the Kolmogorov third-order velocity structure function law [*Kolmogorov*, 1941]. This law is more fundamental than the Kolmogorov $r^{2/3}$ law for the second-order structure function (equivalent to the $k^{-5/3}$ law for spectra) [*Frisch*, 1995; *Lindborg*, 1996]. *Lindborg* [1999] reworked the Kolmogorov analysis to derive theoretical relationships for ideal (i.e., homogeneous, isotropic and non-divergent) 2D turbulence. He then argued that the sign of the third-order structure function D_3 indicates the direction of the cascade: $D_3 < 0$ implies downscale and $D_3 > 0$ implies upscale. *Cho and Lindborg* [2001] found that D_3 was consistent with a downscale energy cascade in the small to intermediate scales, and an upscale energy cascade at the largest scales. Although their results argued against the stratified-upscale theory, in a later paper *Lindborg* [2007] argued against a gravity-wave mechanism and for a stratified-downscale scenario: the atmospheric layers created in stratified turbulence might go unstable due to a shear instability, breaking the layer up into smaller structures, and hence a downscale cascade.

In this paper we apply the Lindborg third-order structure function test to several different QuikSCAT and ASCAT wind products. We find that the third-order results show very good agreement across wind products. Our results also demonstrate that the sign of the third-order structure function varies regionally and seasonally, implying that the question in the first paragraph should not be phrased as 'either-or', but as 'where, when, and why'.

The paper is structured as follows. Structure functions are defined in section 2. In section 3 the scatterometer wind products used are presented. Section 4 describes the study area and methodology. The results are presented and discussed in section 4, and our conclusions are given in section 6.

2 Structure functions

Structure functions are moments of the probability distribution of velocity differences $P_r(\delta u_L, \delta u_T)$ where $\delta u_L = u_L(x_L + r) - u_L(x)$ and $\delta u_T = u_T(x_L + r) - u_T(x)$. The subscript L indicates the longitudinal component and T the transverse component, respectively, the components parallel and perpendicular to the coordinate x_L along which differences are taken. The second-order structure functions are then defined by

$$D_{LL}(r) = \langle \delta u_L \delta u_L \rangle \quad , \quad D_{LT}(r) = \langle \delta u_L \delta u_T \rangle \quad , \quad D_{TT}(r) = \langle \delta u_T \delta u_T \rangle \quad , \tag{1}$$

the diagonal third-order structure functions by

$$D_{LLL}(r) = \left\langle \delta u_L^3 \right\rangle \quad , \quad D_{LTT}(r) = \left\langle \delta u_L \delta u_T^2 \right\rangle \quad , \tag{2}$$

and the off-diagonal structure functions by

$$D_{TTT}(r) = \left\langle \delta u_T^3 \right\rangle \quad , \quad D_{LLT}(r) = \left\langle \delta u_L^2 \delta u_T \right\rangle \quad , \tag{3}$$

with $\langle . \rangle$ denoting an ensemble average.

In ideal turbulence (i.e., homogeneous, isotropic and divergence-free velocity field), $D_{LT}(r) = 0$. Moreover, $D_{TT}(r)$ can be expressed in terms of $D_{LL}(r)$ and $D_{LTTa}(r)$ in terms of $D_{LLL}(r)$. However, the quasi-2D structure of the atmosphere means that the horizontal velocity field is not divergence-free. Therefore, we also use the total second and third-order structure functions, defined for d-dimensional turbulence by

$$D_2(r) = D_{LL}(r) + (d-1)D_{TT}(r) \quad , \tag{4}$$

$$D_3(r) = D_{LLL}(r) + (d-1)D_{LTT}(r) \quad . \tag{5}$$

In the inertial range, the longitudinal and total third-order structure function laws for 3D turbulence are [*Kolmogorov*, 1941; *Lindborg*, 1996; *Antonia et al.*, 1997]

$$D_{LLL}(r) = -\tfrac{4}{5} F_3 r \quad , \tag{6}$$

$$D_3(r) = -\tfrac{4}{3} F_3 r \quad , \tag{7}$$

while for 2D turbulence [*Lindborg and Cho*, 2001]

$$D_{LLL}(r) = -\tfrac{3}{2} F_2 r \quad , \tag{8}$$

$$D_3(r) = -2F_2 r \quad , \tag{9}$$

where F_d is the energy flux. The most important difference between 2D and 3D turbulence is that $F_3 > 0$ (downscale) while $F_2 < 0$ (upscale) [*Lindborg*, 1999].

The total skewness S describes the asymmetry of $P_r(\delta u_L, \delta u_T)$ and is defined by

$$S(r) = \frac{D_3(r)}{D_2^{3/2}(r)} \quad , \tag{10}$$

where use has been made of the second-order structure function law

$$D_2(r) = C_d |F_d|^{2/3} r^{2/3} \quad , \tag{11}$$

with C_d a universal constant. From numerical studies, $C_2 \approx 5.5$ and $C_3 \approx 2$ [*Lindborg*, 1999]. By substituting (11), (9), and (7) into (10), it is easy to show that

$$S_2 \approx 0.15 \quad , \quad S_3 \approx -0.47 \quad , \tag{12}$$

i.e., the total skewness is independent of r.

3 Data

The QuikSCAT satellite was launched by the National Aeronautics and Space Administration (NASA) in June 1999. The mission produced ocean vector winds from July 1999 until November 2009. The MetOp-A satellite was launched in October 2006 and is operated by the European Organisation for the Exploitation of Meteorological Satellites (EUMETSAT). Both satellites are in quasi-sun-synchronous orbits with an inclination angle of $\theta = 98.6^{\mathrm{o}}$. The local times for crossing the equator are about 06:30 (ascending) and 18:30 (descending) for QuikSCAT, and about 09:30 (descending) and 21:30 (ascending) for MetOp-A.

The SeaWinds-on-QuikSCAT scatterometer is a rotating pencil-beam design with an 1800 km wide swath, transmitting at Ku-band (13.4 GHz) [*Tsai et al*., 2000]. The pencil-beam design has a complicated observation geometry that varies across the swath, resulting in a varying performance that is poor in the nadir region and far swath. The ASCAT-on-MetOp-A scatterometer uses a dual-swath fan-beam configuration with two 550 km wide swaths separated by a nadir gap of about 700 km, transmitting at C-band

(5.3 GHz) [*Figa-Saldaña et al.*, 2002]. The fan-beam configuration has constant measurement geometry but varying incidence angle over the swath.

The radar backscatter detected by the scatterometers goes through two levels of processing to produce wind speed and wind direction. Level 1 processing involves averaging individual backscatter measurements on a regularly spaced grid. Level-2 takes the Level-1 data and applies quality control, an inversion step, and an ambiguity removal step. The inversion step uses an empirically derived geophysical model function (GMF) to relate backscatter to the equivalent neutral-stability vector wind at a height of 10 meters. Due to the nature of radar backscatter from the ocean surface, this procedure usually provides multiple solutions referred to as ambiguities. An ambiguity removal algorithm is applied to produce the selected winds.

The wind products used in this paper are the same as used in *King et al.* [2013]. A brief description follows. *ASCAT-12.5* and *ASCAT-25* were produced to Level-1 by EUMETSAT. Level-1 cross-section data are calculated by averaging individual backscatter measurements. The weighting function chosen for this averaging is a two-dimensional Hamming window, designed to provide noise reduction. Level-2 processing is carried out at the Royal Netherlands Meteorological Institute (KNMI) using the ASCAT Wind Data Processor (AWDP). The GMF used in the AWDP is CMOD5.n and ambiguity removal is carried out using a two-dimensional variational method (2DVAR) [*Vogelzang et al.*, 2009].

SeaWinds-NOAA is a near-real-time product that was issued by the National Oceanic and Atmospheric Administration (NOAA) and is described in detail by *Hoffman and Leidner* [2005]. Level-1B processing uses a centroid binning method that assigns a backscatter slice to only one WVC. The GMF is QSCAT-1 and ambiguity removal is carried out using a median filter followed by a sophisticated algorithm called Direction Interval Retrieval with Thresholded Nudging (DIRTH) [*Stiles et al.*, 2002].

SeaWinds-KNMI is a reprocessing of SeaWinds-NOAA by KNMI using improved (rain) quality control [*Portabella and Stoffelen*, 2002]. The GMF is NSCAT-2, and ambiguity removal is carried out using 2DVAR and additional noise reduction by the Multiple Solution Scheme (MSS) [*Vogelzang et al.*, 2009].

QSCAT-12.5 (version 3) is the recently released science data product produced by the NASA Jet Propulsion Laboratory (JPL). It is the result of reprocessing the entire SeaWinds on QuikSCAT dataset with many algorithm improvements [*Fore et al*., 2013]. Level-1B processing uses an overlap binning method that increases the number of backscatter slices being assigned to the same WVC. The GMF is Ku2011 and ambiguity removal is carried out using a median filter followed by an improved DIRTH algorithm.

Rain affects the radar backscatter measured by scatterometers: the higher the radar frequency, the larger the impact of rain attenuation and scattering. As a result, rain is a larger source of error for winds derived from Ku-band instruments (SeaWinds) than from C-band instruments (ASCAT). For example, as many as 16% of wind retrievals from

SeaWinds measurements over the west Pacific warm pool are flagged as rain-contaminated. In contrast, the lower ASCAT radar frequency results in winds that are much less affected by rain, although they are sensitive to secondary effects, such as the splashing of rain drops on the surface and local wind variability when rain is heavy. These secondary effects of rain are a source of `geophysical noise', which at present is not flagged by quality control [*Portabella et al.*, 2012].

To characterize the regional environment, we use rain rates obtained from the Tropical Rainfall Measuring Mission's (TRMM) Microwave Imager (TMI) on board the TRMM satellite. The TMI data were obtained from the Remote Sensing Systems Web site (http://www.ssmi.com). We also use SeaWinds Radiometer (SRAD) rain-rates. These are derived from SeaWinds measurements of the ocean radiometric brightness temperature [*Laupattarakasem et al.*, 2005] and are included with the QuikSCAT 25 km L2B science data product (available from the Physical Oceanography Distributed Data Archive (PO.DAAC)).

4 Study area

The tropical Pacific has both rainy and dry regions. The rainy regions are located over warm pools, defined as the waters enclosed by the 28 °C isotherm [*Wyrtki*, 1989], an empirical threshold for the onset of deep convection, and in regions of strong surface wind convergence: the InterTropical Convergence Zone (ITCZ), the western North

Pacific Monsoon Trough, the South Pacific Convergence Zone (SPCZ), and the Southern-ITCZ, a convergence zone that emerges in the east Pacific from March to April [*Masunaga and L'Ecuyer*, 2010, and references therein]. The dry regions are located in the east Pacific. They are caused by a tongue of cool water brought to the surface by upwelling-favorable winds along South America.

In order to separate rainy and dry regions, while at the same time avoiding Coriolis effects, we selected the region shown in figure 1. It is subdivided into three latitude bands (North, Equatorial, South) and three longitude bands (West, Central and East Pacific). These subregions isolate rainy from dry regions, as can be seen by the latitude time plots of rain rate in figure 2. The nomenclature and latitude-longitude limits of the subregions are given in table 1.

4.1 Application to scatterometer winds

Samples were selected along-swath: WVCs in the same sample all have the same cross-swath index. Each sample was checked to ensure that wind vectors falling outside the subregion of interest or failing quality control were flagged missing. In the case of SeaWinds-NOAA and QSCAT-12.5, wind vectors were flagged missing if the rain flag was set. In the case of ASCAT and SeaWinds-KNMI, wind vectors were flagged missing if the KNMI quality control flag or the variational quality control flag was set [*KNMI*, 2011, section 6.2]. Samples from both the ascending and descending passes of the satellite and from the whole swath (including the outer and nadir parts of the SeaWinds swath) were used to calculate the structure functions.

Velocity differences are taken between members of each along-track sample after transforming wind vectors into components parallel (La) and perpendicular (Ta) to the satellite track, as indicated by the subscript a. One-dimensional along-track structure functions were calculated using the equations in section 2, with ensemble averages defined by

$$\langle . \rangle = \frac{1}{N}\sum_{i=1}^{N}(.) \quad , \tag{13}$$

where N is the number of velocity differences at scale r in a region during a one-month period.

5 Results

Results are interpreted using the framework of 2D turbulence theory so that

$$D_{2a} = D_{LLa} + D_{TTa} \quad , \tag{14}$$

$$D_{3a} = D_{LLLa} + D_{LTTa} \quad , \tag{15}$$

$$S_a = \frac{D_{3a}}{D_{2a}^{3/2}} \quad . \tag{16}$$

5.1 Regional variability of third-order structure functions

The longitudinal and total third-order structure functions D_{LLLa} and D_{3a} for July 2009 are plotted against separation r for all regions in figures 3 and 4, respectively. The difference between the two figures shows that the contribution of D_{LTTa} is minimal in some regions, but significant in others. There are significant differences between the magnitudes obtained from ASCAT and SeaWinds products. These differences are partly due to sampling (QuikSCAT and MetOp-A pass over the same region at different times of the day) and different methods used to process the radar backscatter, with the methods used in ambiguity removal believed to be the most important. Nevertheless the results show a consistent pattern: D_{3a} varies between negative and positive values. In the rainy regions, D_{3a} is negative, except in WPN where $D_{3a} \approx 0$. On the other hand, in the dry regions, $D_{3a} \approx 0$, except in EPE where $D_{3a} > 0$.

The variation in the sign of D_{3a} over the 12 month study period can be investigated more conveniently using the skewness S_a (16). In homogeneous, isotropic turbulence, S_a would be either a positive or negative constant, as given by (12). This gives hope that S_a should vary only weakly with r. This is largely supported by figure 5, where it can be seen that S_a is approximately independent of r in all regions except EPE. There S_a starts negative and rises steeply to positive values by about 100 km, after which it begins to flatten, reaching a constant value at about 500 km. Note that the values attained by S_a vary around the theoretical values given in (12).

After reviewing plots for all regions and months, we concluded that S_a became reasonably independent of r at about 300 km. This scale also corresponds to the upper limit of the scales occupied by meso-β weather phenomena (~ 20 - 300 km), such as squall lines and mesoscale convective systems, giving added importance to this choice. The monthly time series of S_a at $r = 300$ km, hereafter denoted as S_a^*, is shown in figure 6. The figure shows that the magnitude of S_a^* varies only a little with wind product but is consistent in sign. The near equal magnitudes imply that the asymmetry in the shapes of the different wind product velocity difference pdfs $P_r(\delta\mathbf{u})$ at 300 km are approximately equal.

Due to the importance of rain on the quality of scatterometer winds, we adopted the practice of comparing structure function and skewness variability with regional area and monthly-averaged SRAD rain rates. These are shown as bar graphs in each panel of figure 6. The dry regions show an excellent correlation between S_a^* and rain, with S_a^* positive or trending positive during dry seasons and negative or trending negative during wet seasons. The clearest examples are EPE and EPS, due to a wet season lasting only 2-4 months. On the basis of this correlation, one would expect S_a^* to be negative with little variation in magnitude throughout the year. However, this is only true in the ITCZ regions CPN and EPN, where $S_a^* \approx -1$ throughout the year. Surprisingly, the WP regions appear to lack any obvious correlation with rain: in WPN and WPS, S_a^* shows an annual cycle varying between about -1 in winter to near zero in summer; in WPE S_a^* varies between ± 0.2 in phase with WPS.

In summary, we have found that D_{3a}, or S_a , changes sign across the tropical Pacific, providing evidence for both upscale and downscale energy transfer. We also find an intriguing correlation with rain: $S_a^* > 0$ in the dry regions when there is little or no rain, $S_a^* < 0$ in the ITCZ regions (CPN and EPN) all year but only during winter in WPN and WPS. Why S_a^* trends to zero values during summer in WPN and WPS, periods when the regions experience strong convective activity is investigated in the next subsection..

5.2 Energy fluxes

In order to better comprehend the above results, we return to the definition and interpretation of the third-order structure function. Within the framework of turbulence theory, one is led to regard $D_{3a} < 0$ as implying vortices breaking up and $D_{3a} > 0$ as vortices merging. We shall now step away from these iconic images and consider the third-order structure function from a different viewpoint. Rewriting (5) as

$$D_{3a}(r) = \left\langle \delta u_{La} \left[(\delta u_{La})^2 + (\delta u_{Ta})^2 \right] \right\rangle \quad , \tag{17}$$

makes clear that the sign of D_{3a} is linked to the sign of δu_{La}. It is simple to show that if $\delta u_{La} < 0$ ($\delta u_{La} > 0$), then along-track wind components are converging (diverging). Therefore, the analysis should find $D_{3a} < 0$ for regions with strong surface convergence, and $D_{3a} > 0$ for regions with strong surface divergence. Strong surface convergence by deep convection occurs over the WP warm pool regions and ITCZ regions. Strong surface divergence occurs over the cold tongue in EPE when southerly winds blow from cool to warm ocean waters across the strong SST front that forms its northern boundary [*Chelton et al*., 2004; *Small et al*., 2008, and references therein].

When $D_{3a} \approx 0$, this indicates a near-cancellation of terms, suggesting near-equal amounts of convergence and divergence. This could be the result of downdrafts ($\delta u_{La} > 0$) and updrafts ($\delta u_{La} < 0$) as meterological systems pass through the region. To check that possibility, D_{3a} was calculated separately for ascending and descending passes. Figure 7 compares results for WPN and EPS, two regions where $D_{3a} \approx 0$ in figure 4. Results for WPN are shown in the left panels and EPS in the right panels; the top panels show the morning passes and the bottom panels the evening passes. The local time of each pass appears next to the curves in the panels for WPN. Figure 7 shows that large positive-negative swings occur in WPN, whereas only small swings occur in EPS. The latter is consistent with EPS being a region of light and steady winds. However, WPN is a convectively active region. Note that $D_{3a} > 0$ in the cool part of the day (06:30 and 21:30), while $D_{3a} < 0$ in the warm part of the day (09:30 and 18:30). To determine if this might be part of a diurnal cycle, we calculated third-order structure functions using buoy winds measured during the same month in WPN. The results (not shown) reveal fluctuations in magnitude and sign throughout the day and night without clear pattern. Thus the large positive-negative swings are best explained as due to updrafts and downdrafts in mesoscale convective systems known to frequent WPN [*Houze*, 2004]. Furthermore, a review of plots for all regions and all months shows that large positive-negative swings only occur in WPN and only during the months of July and September, indicating that the swings are connected with the seasonal north-south migration of the ITCZ in the west Pacific [*Lander*, 1996, figure 2].

The above results indicate a more dynamic situation where both upscale and downscale energy fluxes are occurring, that would be lost in the usual averaging process. With this in mind, we now turn our attention to the estimation of energy fluxes. In the following it is more convenient to work with the longitudinal structure function D_{LLLa} and its density,

$$d_{LLLa}(r, \delta u_{La}) = [\delta u_{La}(r)]^3 P_r(\delta u_{La}) \quad , \tag{18}$$

where $P_r(\delta u_{La})$ is the empirical probability distribution function constructed from all δu_{La} at separation r in a given region and month. In fact, it is more interesting to calculate the energy flux defined using (8) by

$$F_a = \frac{D_{LLLa}}{r} \quad , \tag{19}$$

where the minus sign and constant multiplying F_2 in (8) is absorbed into the definition of F_a, and the energy flux density

$$f_a = \frac{d_{LLLa}}{r} \quad , \tag{20}$$

The fluxes presented in the following figures are estimates obtained by averaging the fluxes calculated at r = 100, 200, and 300 km.

Figure 8 shows how the energy flux density is distributed with δu_{La} in the month of July in each region. Note that the ITCZ regions, CPN and EPN, are plotted using a different scale. The figure shows that upscale and downscale energy flux is concentrated into a narrow range of δu_{La}. Systematic differences between ASCAT and SeaWinds can be easily seen. In the rainy regions, SeaWinds has a peak at smaller δu_{La} and with reduced amplitude compared to ASCAT. Yet another difference can be seen for the NOAA product in CPS and EPS, where the upscale energy is distributed across a larger range of δu_{La}. This feature is attributed to the larger noise component in the NOAA product.

Figure 9 shows the integrated flux split into upscale flux ($F_a^+ > 0$, $\delta u_{La} > 0$) and downscale flux ($F_a^- < 0$, $\delta u_{La} < 0$) as monthly time series for each region. As in the previous figure, the ITCZ regions are plotted with a different scale. The figure shows that there is upscale flux in all months in all regions, with the largest upscale fluxes in WP regions during the convectively active seasons. Interestingly, the WP upscale fluxes are as large as or larger than that found for EPE. As indicated in the previous figure, ASCAT fluxes are larger than SeaWinds fluxes, with the largest differences occurring in the rainy regions and rainy months of the dry season.

6 Conclusions

In this paper we have calculated one-dimensional longitudinal (D_{LLLa}) and total ($D_{3a} = D_{LLLa} + D_{LTTa}$) third-order structure functions using along-track winds at the bottom of the marine boundary layer inferred from radar backscatter measurements by the SeaWinds-on-QuikSCAT and ASCAT-on-MetOp-A scatterometers. The region studied was the tropical Pacific, subdivided into rainy and dry regions. The study period was November 2008 - October 2009, a period when both scatterometers were operational.

According to turbulence theory, the sign of the third-order structure function identifies the direction of energy flux, with $D_{3a} < 0$ implying downscale flux and $D_{3a} > 0$ upscale flux. We monitored the mesoscale behavior of D_{3a} using the skewness at 300 km (S_a^*), enabling a concise representation in terms of a monthly time series for each region. We found that S_a^* varied regionally and seasonally in magnitude and sign. Comparison with regional monthly rain-rates showed an excellent correlation with skewness in dry regions, with positive skewness in rain-free months and negative values during rainy months.

A more complicated relationship with rain was found for the west Pacific regions. This led to the estimation of upscale and downscale energy fluxes using the third-order structure function law, which revealed a large component of upscale energy flux in the west Pacific regions during convectively active seasons. Moreover, it was shown that in every month in every region there is a certain fraction of the flux that is upscale, with regions of largest upscale flux over the cold tongue (EPE) during the cold season, and in the west Pacific regions (WPN, WPE and WPS) during their convectively active season. The ITCZ regions (CPN and EPN) had the largest downscale flux, with maximum values in boreal winter, a secondary maximum in May-June, minimum in March and a secondary minimum in August-September.

The standard picture of energy transfer in 3D turbulence is that energy is drained from larger to smaller scales via vortex folding and stretching. In ideal 2D turbulence the actual mechanism remains controversial, but numerical studies indicate that it involves the coupling of the large-scale stress to the thinning of smaller-scale vortices [*Boffetta and Ecke*, 2012]. The results in this paper are difficult to interpret in terms of a 3D or 2D process. Instead, we have the following interpretation. The downscale energy flux represents the energy transported out of the surface layer partly into the ocean, say, as wind-driven waves, and partly transported vertically upwards by convection. The upscale energy flux represents the energy transported into the surface layer by low-level divergence created by downdrafts in storms or, as in the east Pacific, by spatial acceleration of winds across a strong SST gradient. An additional contribution to upscale flux may come from wave-driven-winds [*Hanley et al*., 2010].

Our results reflect strong ocean-atmosphere interaction, effects missed in upper troposphere / lower stratosphere aircraft measurements. We find that atmospheric turbulence in the mesoscales transfers kinetic energy both upscale and downscale, but in a process that is neither like 3D nor 2D turbulence.

Acknowledgements

This work has been funded by EUMETSAT in the context of the NWP SAF part of the SAF network. The contribution of GPK has been supported by EUMETSAT under the visiting scientist programme.

References

Antonia, R.A., M. OuldRouis, F. Anselmet, and Y. Zhu (1997), Analogy between predictions of Kolmogorov and Yaglom, *J. Fluid Mech., 332*, 395-409.

Boffetta, G., and R.E. Ecke (2012), Two-Dimensional Turbulence, *Annu. Rev. Fluid Mech., 44*, 427-451, doi:10.1146/annurev-fluid-120710-101240.

Charney, J.G. (1971), Geostrophic turbulence, *J. Atmos. Sci., 28*, 1087-1095.

Chelton, D. B., M. G. Schlax, M. H. Freilich, and R. F. Milliff (2004), Satellite Measurements Reveal Persistent Small-Scale Features in Ocean Winds, *Science, 303* (5660), 978-983, doi:10.1126/science.1091901.

Cho, J. Y. N., and E. Lindborg (2001), Horizontal velocity structure functions in the upper troposphere and lower stratosphere, 1. Observations, *J. Geophys. Res., 106* (*D10*), 10,223-10,232, doi:10.1029/2000JD900814.

Dewan, E. (1997), Saturated-cascade similitude theory of gravity wave spectra, *J. Geophys. Res. - Atmos., 102*, 29,799-29,817.

Dewan, E.M. (1979), Stratospheric wave spectra resembling turbulence, *Science, 204*, 832.

Figa-Saldaña, J., J. Wilson, E. Attema, R. Gelsthorpe, M. Drinkwater, and A. Stoffelen (2002), The advanced scatterometer (ASCAT) on the meteorological operational (MetOp) platform: A follow on for the European wind scatterometers, *Can. J. Remote Sens., 28*, 404-412, doi:10.5589/m02-035.

Fore, A., B. Stiles, A. Chau, B. Williams, R. Dunbar, and E. Rodr\'iguez (2013), Point-Wise Wind Retrieval and Ambiguity Removal Improvements for the QuikSCAT Climatological Data Set, *IEEE Trans. Geosci. Remote Sens., PP*(*99*), 1-9, doi:10.1109/TGRS.2012.2235843.

Freilich, M. H., and D. B. Chelton (1986), Wavenumber spectra of Pacific winds measured by the Seasat scatterometer, *J. Phys. Oceanogr., 16*, 751-757.

Frisch, U. (1995), *Turbulence: The legacy of A. N. Kolmogorov*, 296 pp., Cambridge University Press.

Gage, K. S. (1979), Evidence for a $k^{-5/3}$ law inertial range in mesoscale two-dimensional turbulence, *J. Atmos. Sci., 36*, 1950-1954.

Hanley, K. E., S. E. Belcher, and P. P. Sullivan (2010), A global cimatology of wnd-wave interaction, *J. Phys. Oceanogr., 40* (6), 1263-1282, doi:10.1175/2010JPO4377.1.

Hoffman, R. N., and S. M. Leidner (2005), An introduction to the near-real-time QuikSCAT data, *Wea. Forecasting, 20*, 476-493, oi:10.1175/WAF841.1.

Houze, R. A. (2004), Mesoscale convective systems, *Rev. Geophys., 42*, RG4003, doi:10.1029/2004RG000150.

King, G. P., J. Vogelzang, and A. Stoffelen (2013), Second-order structure function analysis of scatterometer winds over the tropical Pacific: Part 2. Rainy and dry regions, *Tech. rep.*, NWPSAF-KN-VS-012, EUMETSAT.

KNMI (2011), ASCAT Wind Product User Manual.

Kolmogorov, A. N. (1941), Dissipation of energy in locally isotropic turbulence, *Dokl. Akad. Nauk. SSSR, 32*, 19-21.

Lander, M. A. (1996), Specific tropical cyclone track types and unusual tropical cyclone motions associated with a reverse-oriented monsoon trough in the western North Pacific, *Wea. Forecasting, 11*(2), 170-186, doi:10.1175/1520-0434(1996)011<0170:STCTTA>2.0.CO;2.

Laupattarakasem, P., W. Jones, K. Ahmad, and S. Veleva (2005), Calibration/validation of the SeaWinds radiometer rain rate algorithm, in *OCEANS, 2005. Proceedings of MTS/IEEE*, vol. 3, pp. 2601-2604, doi:10.1109/OCEANS.2005.1640163.

Lilly, D. K. (1983), Stratified turbulence and the mesoscale variability of the atmosphere, *J. Atmos. Sci., 40*, 749-761.

Lilly, D. K. (1989), Two-dimensional turbulence generated by energy sources at two scales, *J. Atmos. Sci., 46*, 2026-2030.

Lindborg, E. (1996), A note on Kolmogorov's third-order structure-function law, the local isotropy hypothesis and the pressure-velocity correlation, *J. Fluid Mech., 326*, 343-356.

Lindborg, E. (1999), Can the atmospheric kinetic energy spectrum be explained by two-dimensional turbulence?, *J. Fluid Mech., 388*, 259-288.

Lindborg, E. (2007), Horizontal wavenumber spectra of vertical vorticity and horizontal divergence in the upper troposphere and lower stratosphere, *J. Atmos. Sci., 64* (3), 1017-1025, doi:10.1175/JAS3864.1.

Lindborg, E., and J. Y. N. Cho (2001), Horizontal velocity structure functions in the upper troposphere and lower stratosphere, 2. Theoretical considerations, *J. Geophys. Res., 106* (D10), 10,233-10,241, doi:10.1029/2000JD900815.

Masunaga, H., and T. S. L'Ecuyer (2010), The southeast Pacific warm band and double ITCZ, *J. Climate, 23*, 1189-1208, doi:10.1175/2009JCLI3124.1.

Nastrom, G. D., and K. S. Gage (1985), A climatology of atmospheric wavenumber spectra of wind and temperature observed by commercial aircraft, *J. Atmos. Sci., 42*, 950-960.

Nastrom, G. D., K. S. Gage, and W. H. Jasperson (1984), Kinetic energy spectrum of large-and mesoscale atmospheric processes, *Nature, 310*, 36-38, doi:10.1038/310036a0.

Patoux, J., and R. A. Brown (2001), Spectral analysis of QuikSCAT surface winds and two-dimensional turbulence, *J. Geophys. Res., 106* (D20), 23,995-24,005, doi:10.1029/2000JD000027.

Portabella, M., and A. Stoffelen (2002), A comparison of KNMI Quality Control and JPL Rain Flag for SeaWinds, *Can. J. Remote Sens., 28*, 424-430.

Portabella, M., A. Stoffelen, W. Lin, A. Turiel, A. Verhoef, J. Verspeek, and J. Ballabrera-Poy (2012), Rain effects on ASCAT retrieved winds: Towards an improved quality control, *IEEE Trans. Geosci. Remote Sens., 50*, 2495-2506, doi:10.1109/TGRS.2012.2185933.

Rodriguez, E., and A. Chau (2011), Improved wind directions, divergence, vorticity and their spectra for the QuikSCAT scatterometer, J. Geophys. Res. ??????

Small, R. J., S. deSzoeke, S. Xie, L. O'Neill, H. Seo, Q. Song, P. Cornillon, M. Spall, and S. Minobe (2008), Air-sea interaction over ocean fronts and eddies, *Dyn. Atmos. Oceans, 45*, 274-319.

Stiles, B., B. Pollard, and R. Dunbar (2002), Direction interval retrieval with thresholded nudging: A method for improving the accuracy of QuikSCAT winds, *IEEE Trans. Geosci. Remote Sens., 40*, 79-89.

Tsai, W.-T., M. Spencer, C. Wu, C. Winn, and K. Kellogg (2000), SeaWinds on QuikSCAT: sensor description and mission overview, in *Geoscience and Remote Sensing Symposium, 2000. Proceedings. IGARSS 2000. IEEE 2000 International*, vol. 3, pp. 1021 -1023 vol.3, doi:10.1109/IGARSS.2000.858008.

Van Zandt, T. E. (1982), A} universal spectrum of buoyancy waves in the atmosphere, *Geophys. Res. Lett., 9*, 575-578.

Vogelzang, J., A. Stoffelen, A. Verhoef, J. de Vries, and H. Bonekamp (2009), Validation of two-dimensional variational ambiguity removal on SeaWinds scatterometer data, *J. Atmos. Oceanic Technol., 26*, 1229-1245, doi:10.1175/2008JTECHA1232.1.

Wikle, C. K., R. F. Milliff, and W. G. Large (1999), Surface wind variability on spatial scales from 1 to 1000 km observed during TOGA COARE, *J. Atmos. Sci., 56*, 2222-2231.

Wyrtki, K. (1989), Some thoughts about the west Pacific warm pool, in *Proceedings of the Western Pacific International Meeting and Workshop on TOGA COARE*, edited by J. Picaut, R. Lucas, and T. Delcroix, pp. 99-109, New Caledonia, ORSTUM, Centre de Nouma.

Xu, Y., L.-L. Fu, and R. Tulloch (2011), The global characteristics of the wavenumber spectrum of ocean surface wind, *J. Phys. Oceanogr., 41*, 1576-1582, doi:10.1175/JPO-D-11-059.1.

Figure captons

Figure 1. The boundaries of the nine geographical regions studies in this paper. The nomenclature and geographical limits are given in table 1. Some SeaWinds ascending swaths are shown in grey.

Figure 2. Latitude-time plots of monthly and zonally average rain rate measured by the TRMM Microwave Imager (TMI) during the study period November 2008 – October 2009.

Figure 3. Regional variability of D_{LLLa} in July 2009.

Figure 4. Regional variability of D_{3a} in July 2009.

Figure 5. Regional variability of the skewness $S_a(r)$ in July 2009.

Figure 6. Time series of the skewness at 300 km, S_a^*. The bar graph shows the monthly averaged SRAD rain rates in mm/hr, as indicated by the right hand axes.

Figure 7. Comparison of D_{3a} for the morning and evening passes in WPN (left hand panels) and EPS (right hand panels) in July 2009. Note that the QuikSCAT satellite crosses the equator at 06:30 and 18:30, while MetOp-A crosses three hours later at 09:30 and 21:30. Curves as in figure 6.

Figure 8. Flux density f_a in units of 10^{-6} m^2s^{-3} against δu_{La}.Fluxes are estimated using the third-order structure function law. Note that CPN and EPN are plotted at a different scale.

Figure 9. The upscale (positive) and downscale (negative) fluxes. Note that CPN and EPN are plotted at a different scale.

Table 1. Geographical limits and nomenclature for the study regions shown in figure 1.

	West Pacific 140 °E – 180 °E	Central Pacific 180 °E – 220 °E	East Pacific 220 °E – 260 °E
North 5 °N – 10 °N	WPN (Rainy)	CPN (Rainy)	EPN (Rainy)
Equatorial 5 °S – 5 °N	WPE (Rainy)	CPE (Dry)	EPE (Dry)
South 5 °S – 10 °S	WPS (Rainy)	CPS (Dry)	EPS (Dry)

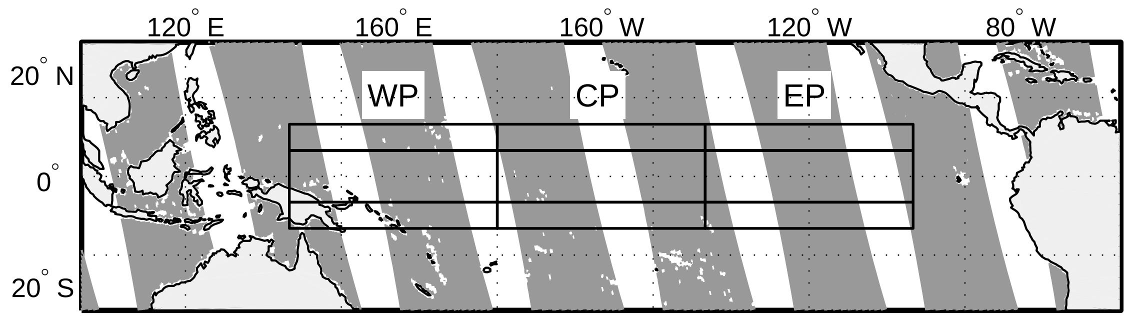

Figure 1. The boundaries of the nine geographical regions studies in this paper. The nomenclature and geographical limits are given in table 1. Some SeaWinds ascending swaths are shown in grey.

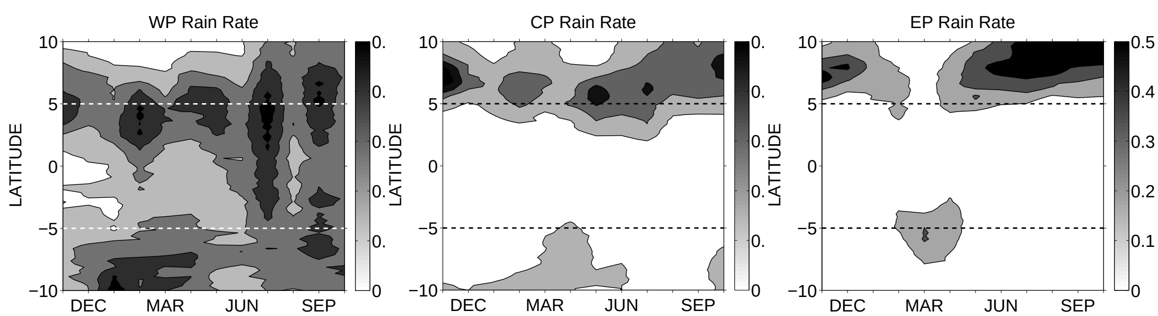

Figure 2. Latitude-time plots of monthly and zonally average rain rate measured by the TRMM Microwave Imager (TMI) during the study period November 2008 – October 2009.

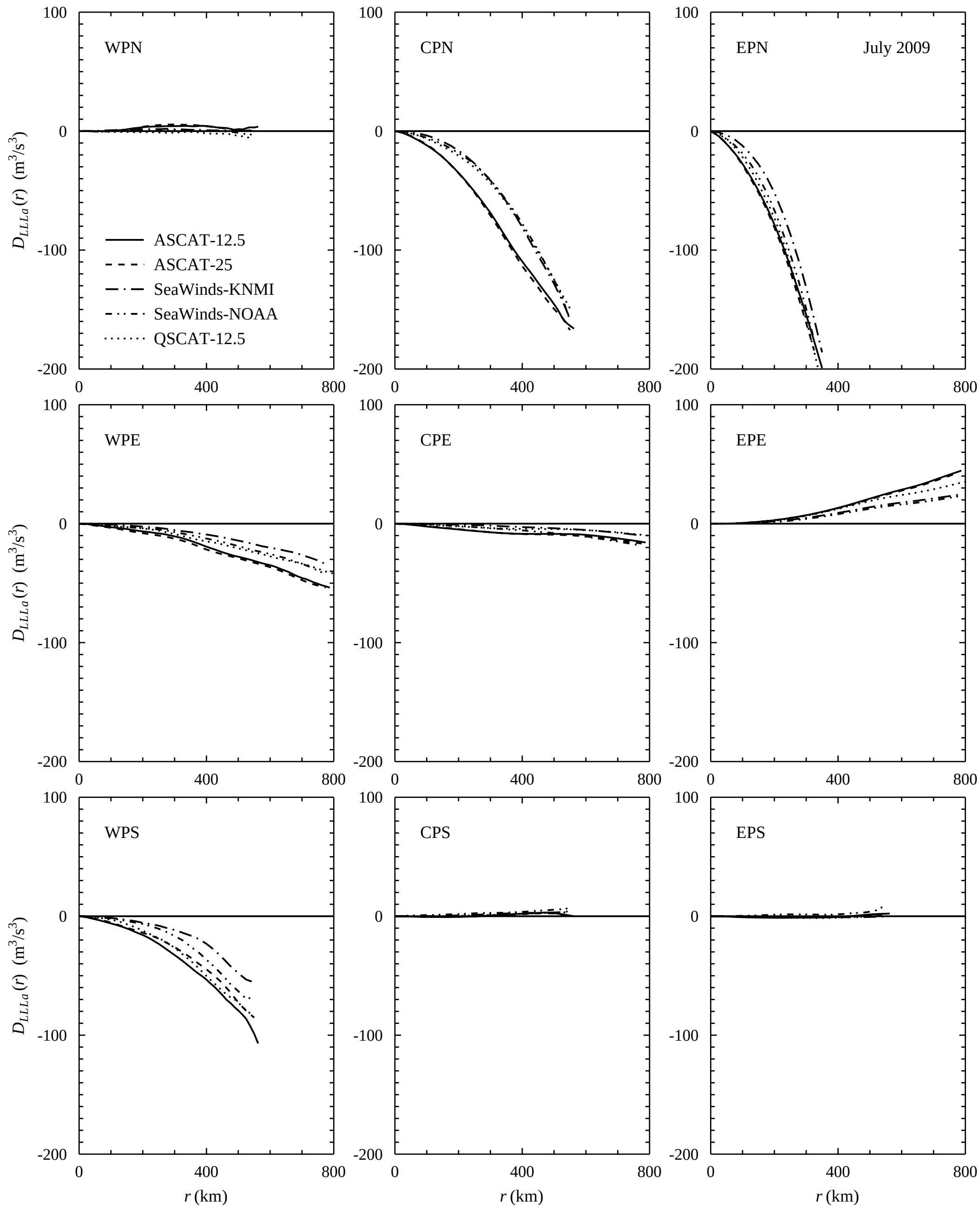

Figure 3. Regional variability of D_{LLLa} in July 2009.

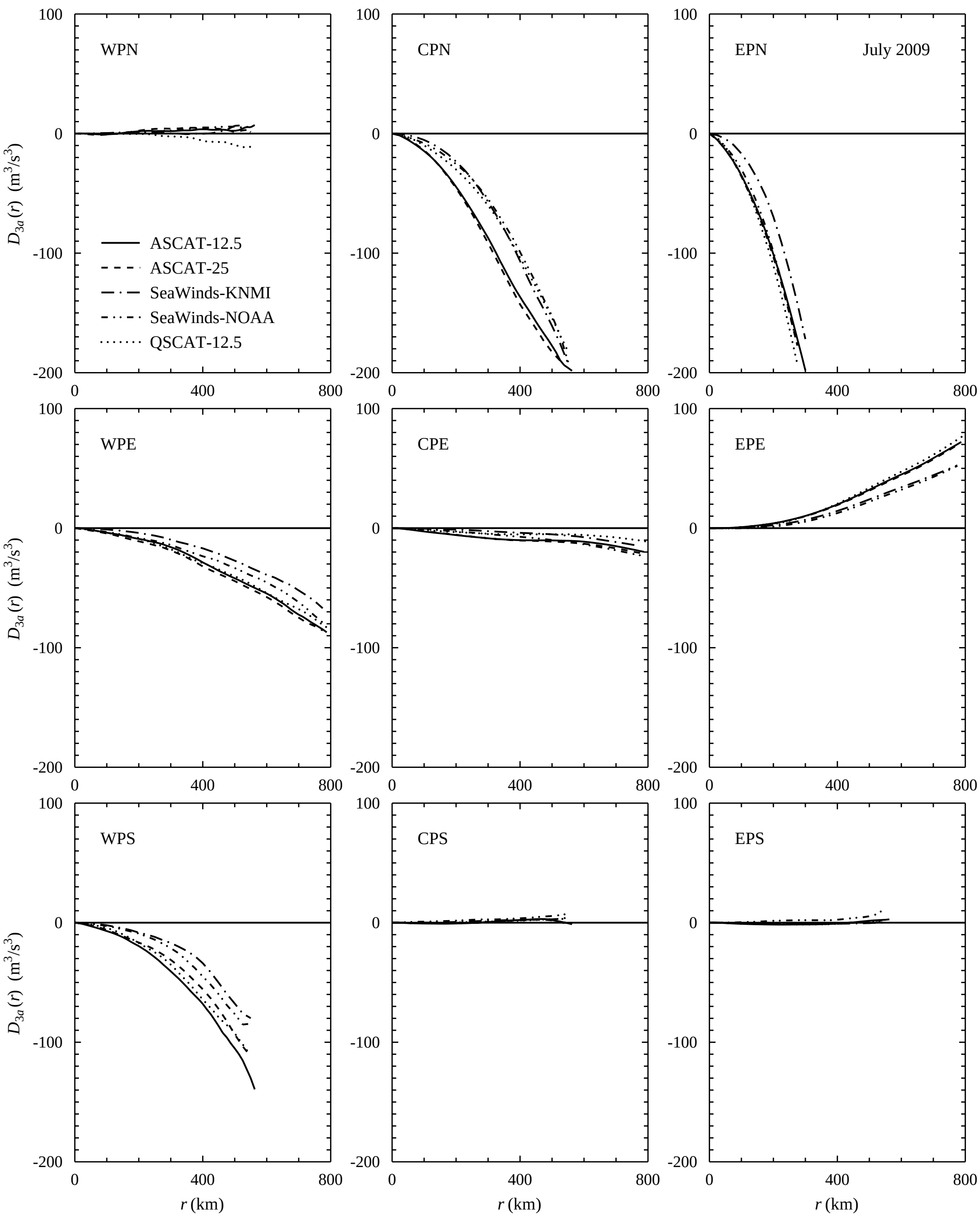

Figure 4. Regional variability of D_{3a} in July 2009.

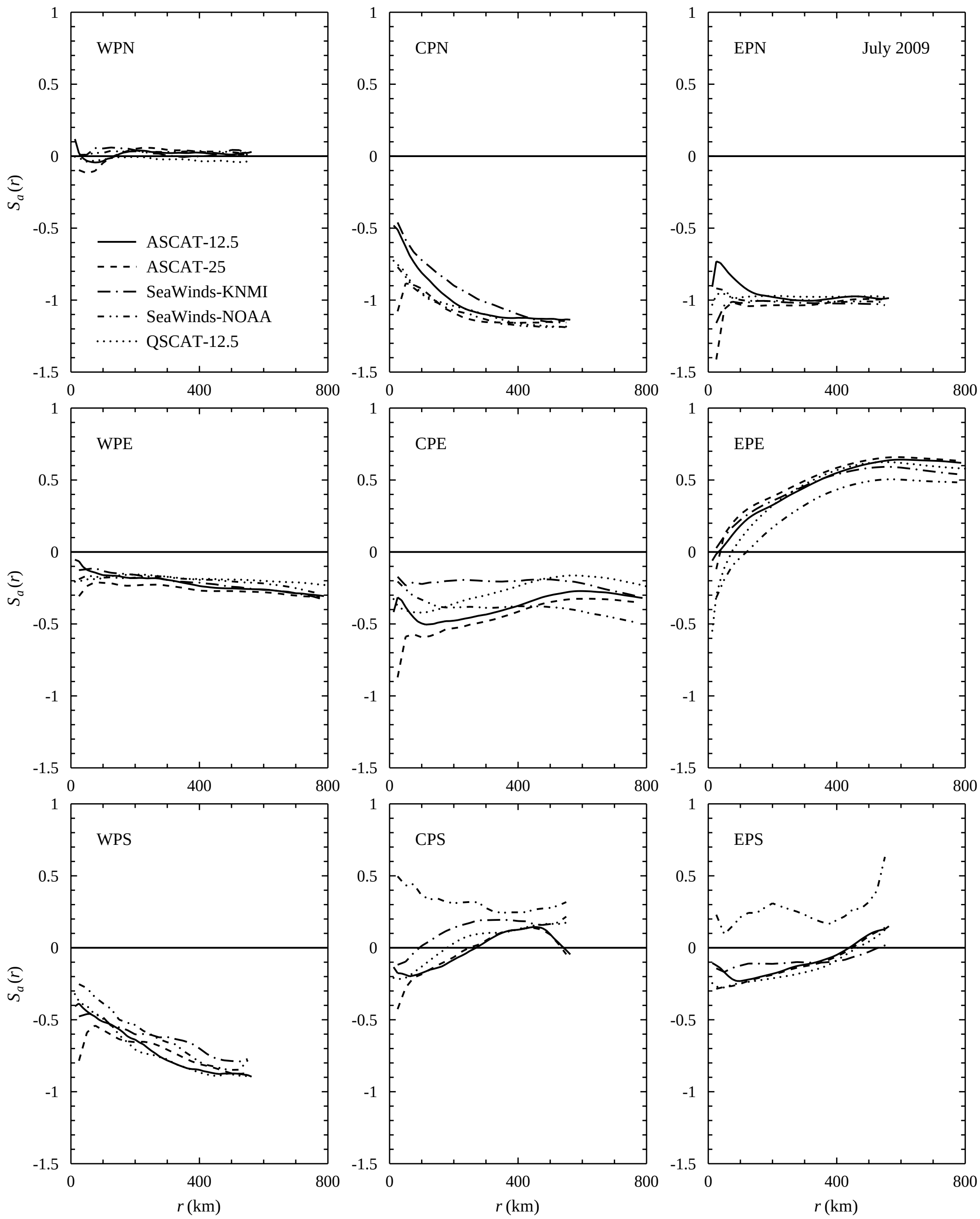

Figure 5. Regional variability of the skewness $S_a(r)$ in July 2009.

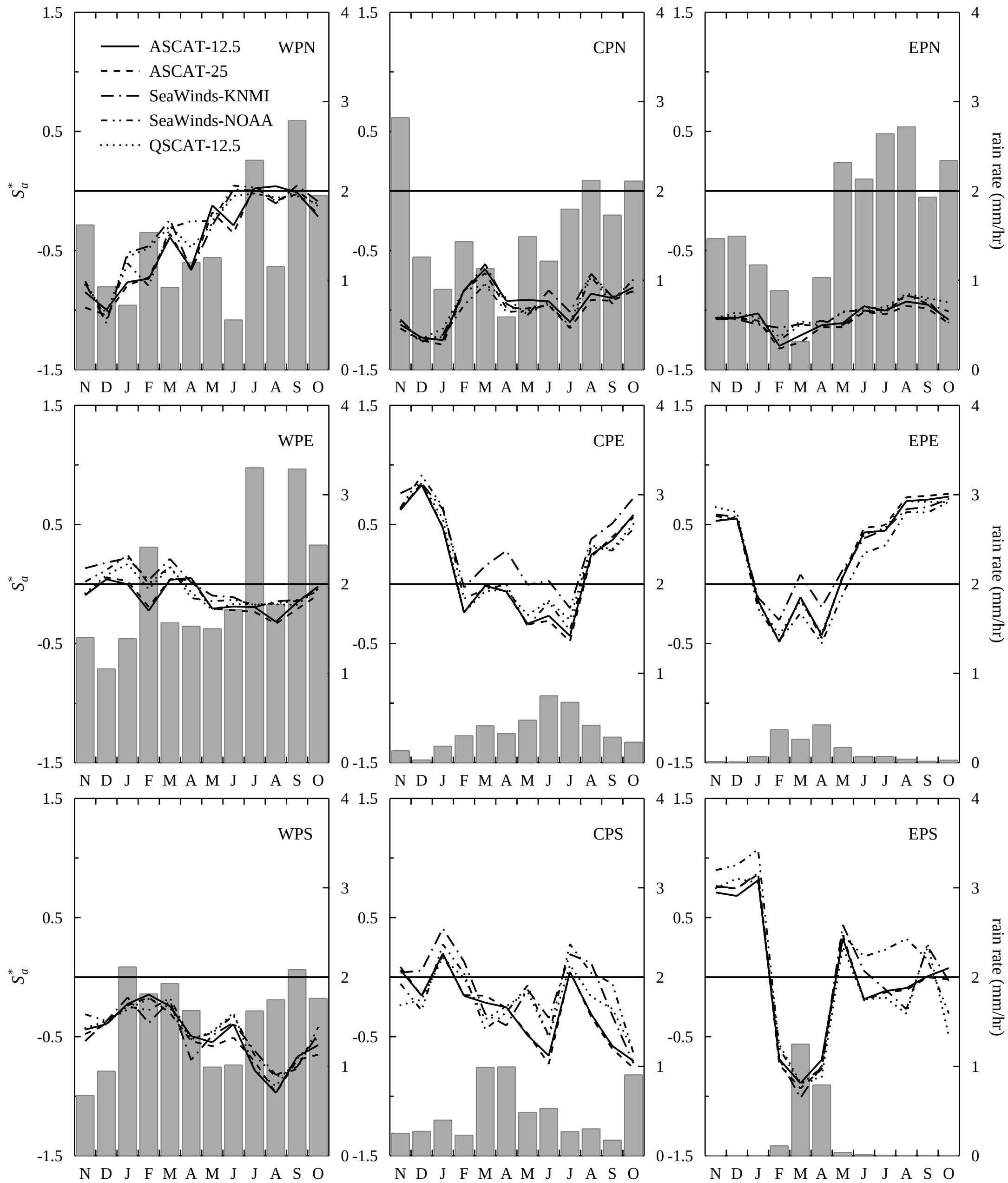

Figure 6. Time series of the skewness at 300 km, S_a^*. The bar graph shows the monthly averaged SRAD rain rates in mm/hr, as indicated by the right hand axes.

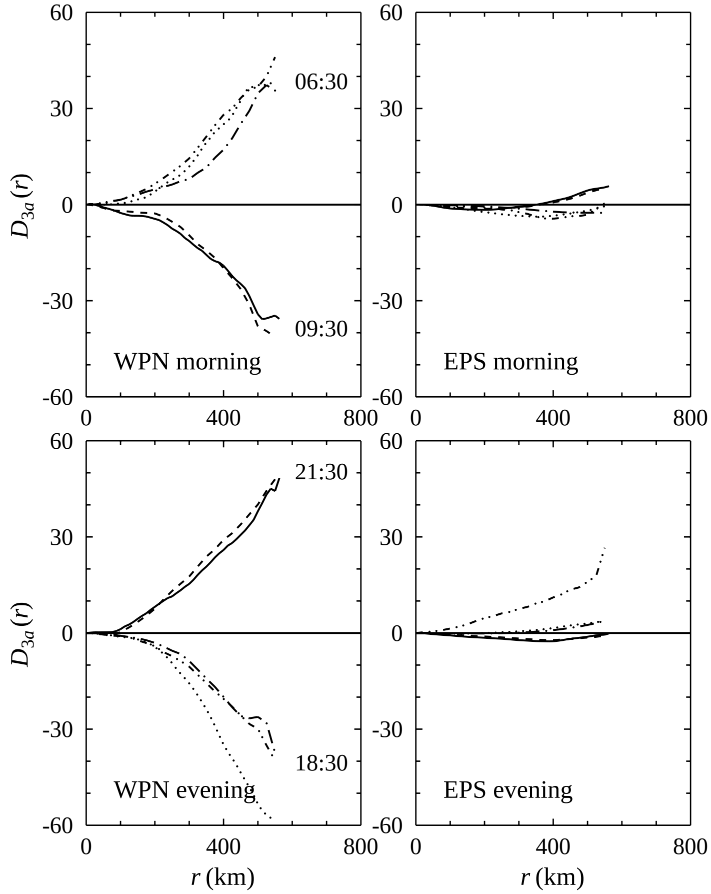

Figure 7. Comparison of D_{3a} for the morning and evening passes in WPN (left hand panels) and EPS (right hand panels) in July 2009. Note that the QuikSCAT satellite crosses the equator at 06:30 and 18:30, while MetOp-A crosses three hours later at 09:30 and 21:30. Curves as in figure 6.

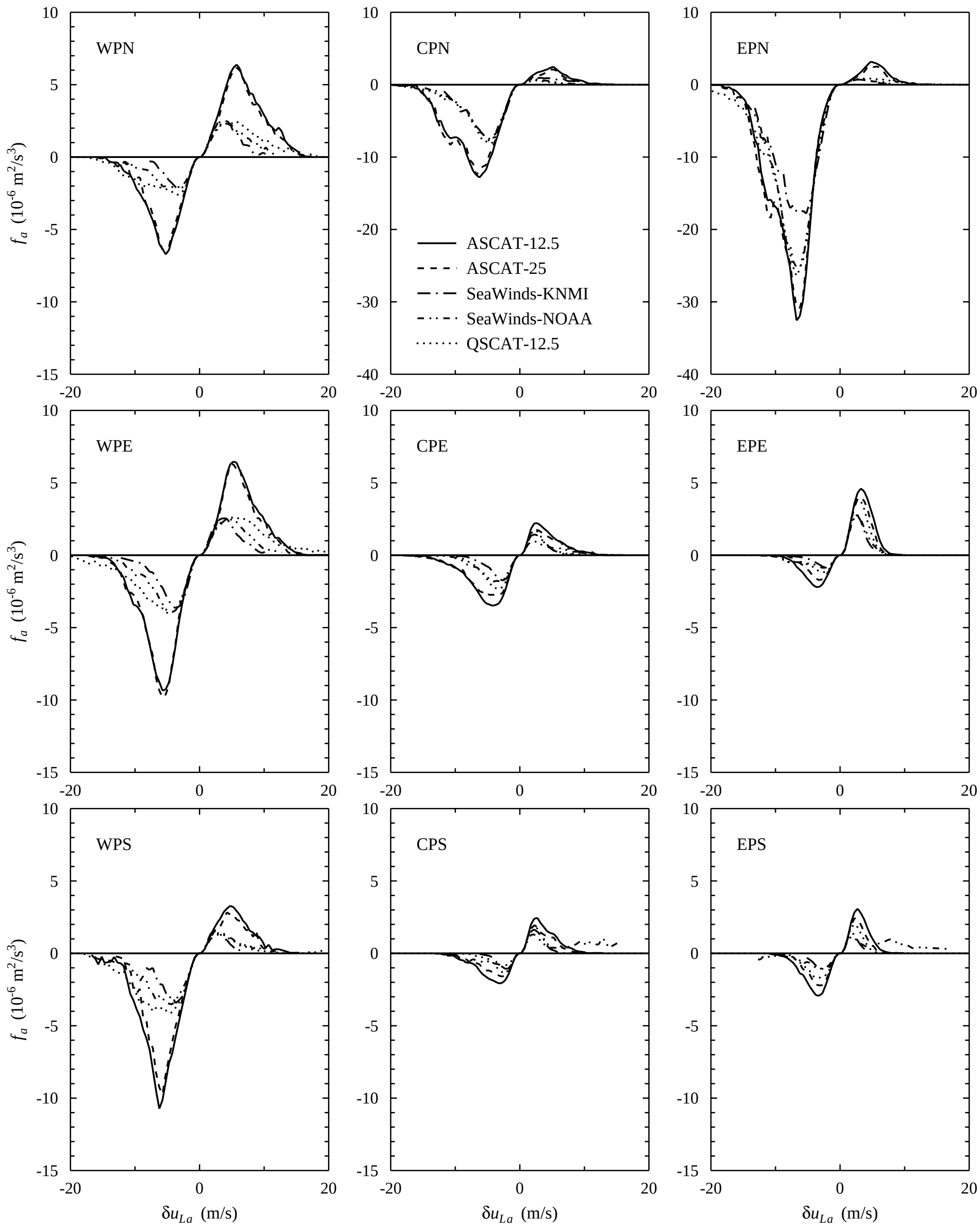

Figure 8. Flux density f_a in units of 10^{-6} m^{2}s^{-3} against δu_{La} .Fluxes are estimated using the third-order structure function law. Note that CPN and EPN are plotted at a different scale.

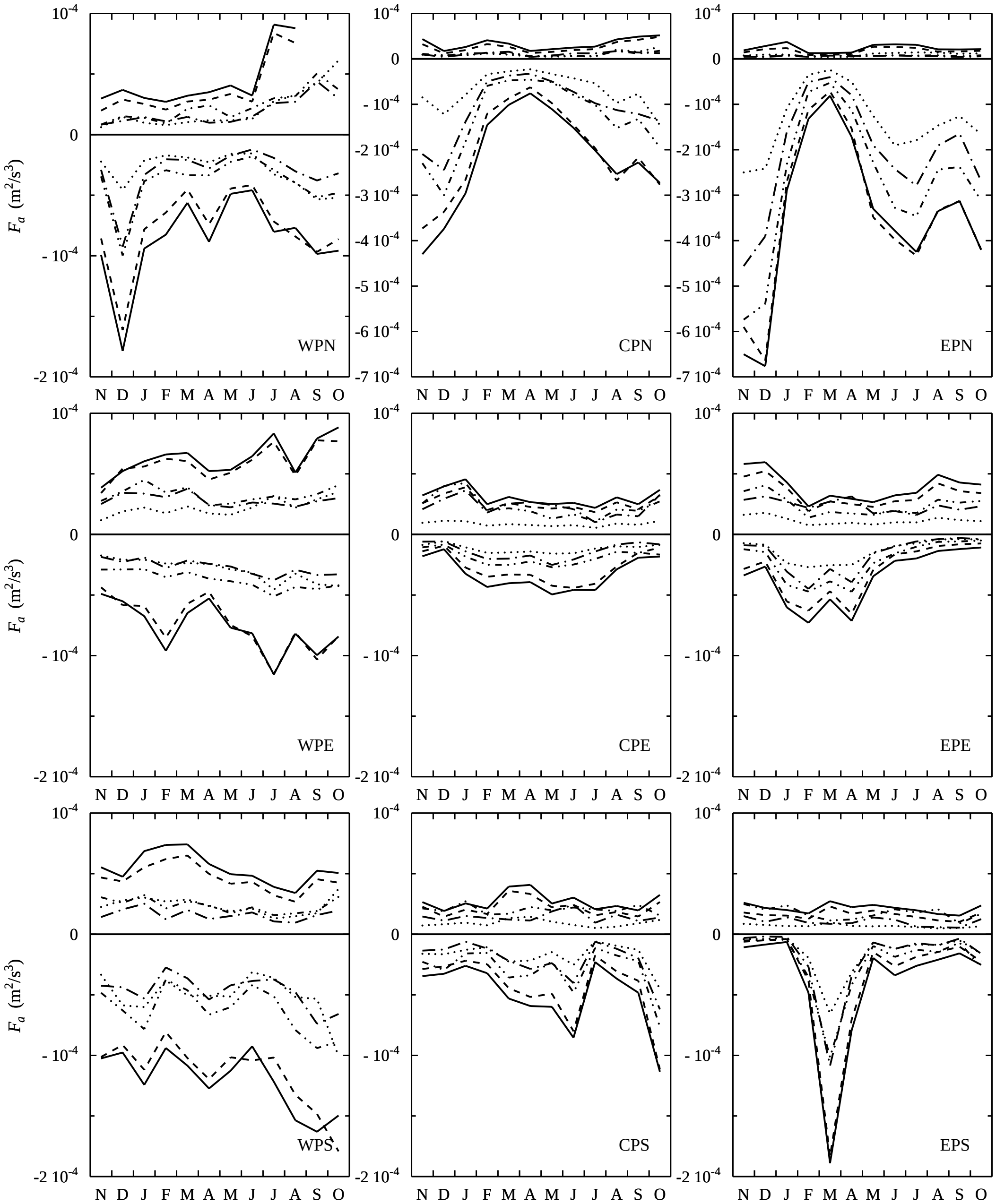

Figure 9. The upscale (positive) and downscale (negative) fluxes. Note that CPN and EPN are plotted at a different scale.